Matter

CellPress

Article

Natural SEI-Inspired Dual-Protective Layers via Atomic/Molecular Layer Deposition for Long-Life Metallic Lithium Anode

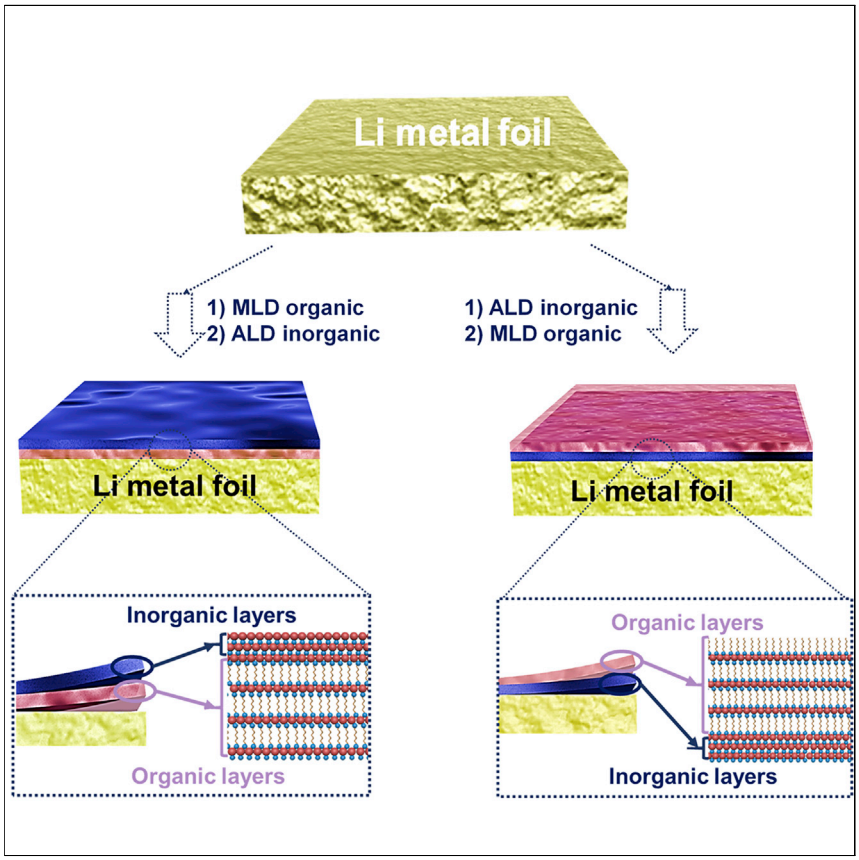

An SEI-inspired dual protective layer is proposed for Li metal anode with rationally designed and highly controllable structures and robust mechanical properties (the organic alucone as the outer layer and inorganic Al_2O_3 as the inner layer), which is precisely controlled by atomic layer deposition (ALD) and molecular layer deposition (MLD) techniques. The SEI-inspired dual layer protected Li metal anode by ALD and MLD realizes stable electrochemical performances and suppressed mossy/dead Li growth.

Yang Zhao, Maedeh Amirmaleki, Qian Sun, ..., Tobin Filleter, Mei Cai, Xueliang Sun

filleter@mie.utoronto.ca (T.F.)
mei.cai@gm.com (M.C.)
xsun@eng.uwo.ca (X.S.)

HIGHLIGHTS

A novel concept of "dual protective layers" is demonstrated for Li metal anode

The unique properties of the dual layers are precisely controlled by ALD/MLD

Ultralong-lifetime Li anode is achieved with SEI-inspired dual protective layer

The mechanical properties of the dual layers are studied by AFM deflection tests

Improvement
Enhanced performance with innovative design or material control

Zhao et al., Matter 1, 1215–1231
November 6, 2019 © 2019 Published by Elsevier Inc.
https://doi.org/10.1016/j.matt.2019.06.020

Matter

CellPress

Article

Natural SEI-Inspired Dual-Protective Layers via Atomic/Molecular Layer Deposition for Long-Life Metallic Lithium Anode

Yang Zhao,[1,5] Maedeh Amirmaleki,[4,5] Qian Sun,[1] Changtai Zhao,[1] Anastasia Codirenzi,[3] Lyudmila V. Goncharova,[3] Changhong Wang,[1] Keegan Adair,[1] Xia Li,[1] Xiaofei Yang,[1] Feipeng Zhao,[1] Ruying Li,[1] Tobin Filleter,[4,*] Mei Cai,[2,*] and Xueliang Sun[1,6,*]

SUMMARY

The solid electrolyte interphase (SEI) layer is one of the key factors for Li metal anode affecting the Li-deposition behavior and electrochemical performances. However, the fabrication of artificial SEI layers with precisely controlled composition, thickness, and mechanical properties is still challenging and difficult to be realized. In this study, we demonstrate an SEI-inspired dual protective layer for Li metal anode with highly controllable structures and robust mechanical properties (the organic alucone as the outer layer and inorganic Al_2O_3 as the inner layer), which is deposited by atomic layer deposition (ALD) and molecular layer deposition (MLD) techniques. The dual-layer protected Li anode displays significantly enhanced electrochemical performances, suppressed mossy/dead Li formation, and robust properties during the plating/stripping process. It is believed that our design of dual-layer protected Li metal anode by ALD and MLD opens up new opportunities for the realization of next-generation high-energy-density Li metal batteries.

INTRODUCTION

Next-generation Li metal batteries, including Li-S, Li-air, and all-solid-state Li metal batteries, have received increasing attention in recent years due to their higher energy densities compared with conventional Li-ion batteries.[1–4] The Li metal anodes are considered as the "Holy Grail" for the next-generation Li metal batteries with high theoretical capacity, low electrochemical potential, and light weight. However, the Li metal anode still has several major challenges to be addressed before practical applications.[5–7] First, the mossy-like and dendritic Li growth is widely observed and reported as one of the main challenges during the electrochemical plating/stripping process.[8,9] The serious Li dendrite growth also leads to various issues, including the safety concerns caused by the internal short-circuiting with Li dendrite penetration and the increased surface area that leads to accelerated side reactions.[10,11] Second, "dead Li" layer formation is another issue caused by the non-uniform nucleation, growth, and stripping of Li metal that promotes the development of anisotropic regions of electronically isolated Li metal.[12] This electrochemically inert "dead Li" layer will decrease the Coulombic efficiency (CE) and increase the diffusion pathway, leading to the large Li-ion diffusion and electronic resistances with large polarization and unsatisfactory energy efficiency.[13,14]

During the Li electrochemical deposition process, the solid electrolyte interphase (SEI) layer is a critical component formed by the chemical/electrochemical reaction

Progress and Potential

Next-generation Li metal batteries have received increasing attention due to their higher energy densities compared with conventional Li-ion batteries. The Li metal anodes are considered as the "holy grail" for the Li metal batteries with high theoretical capacity, low electrochemical potential, and light weight. However, the Li metal anode still has several major challenges before commercialization. Here, we demonstrate the natural solid electrolyte interphase-inspired dual protective layers for highly stable Li metal anodes with rationally designed and precisely controlled compositions and thicknesses by atomic layer deposition (ALD) and molecular layer deposition (MLD). The dual protective layer can significantly enhance the cycling stability and extend the life for Li metal anodes. It is believed that our designs by ALD and MLD may open up new opportunities for the realization of the next-generation high-energy-density Li metal batteries.

between liquid electrolytes and Li metal.[15–17] The unstable SEI layer with non-uniform Li^+ flux distribution can promote the dendrite growth, whereby the collapse of the SEI film can lead to the non-homogeneous local current buildup and non-homogeneous nucleation.[18,19] In this case, significant efforts have been attempted to create artificial SEI layers to stabilize the interface of Li metal anode and achieve enhanced performances.[20–23] Different protective layers have been developed, including inorganic metal oxide,[24,25] metal sulfides,[26] solid-state electrolytes,[27–29] and polymer films.[30–33] It is believed that the compositions, structures, and thicknesses of the artificial SEI are essential for the electrochemical performances of the Li metal anode. Previous studies have shown that the naturally formed SEI on Li metal generally consists of two layers, including the inner inorganic layer close to the Li surface (such as Li_2O, Li_3N, LiF, LiOH, and Li_2CO_3) and outer organic layer with higher oxidation states (such as $ROCO_2Li$, ROLi, and $RCOO_2Li$).[34,35] This natural SEI layer is generally non-homogeneous with respect to both thickness and composition, leading to the performance's degradations of the Li metal anode. However, the structure of this naturally formed SEI provides promising features as an interfacial layer on the Li metal anode. On one hand, the outer porous organic layer can provide rapid Li-ion diffusion from the liquid electrolyte as well as flexibility to relieve the volume change.[34] On the other hand, the inorganic layer with electronic insulation can prevent the transfer of electrons from the Li metal to the electrolyte, further blocking the electrochemical reduction of electrolyte components. Inspired by the naturally formed SEI, the multilayer structures of artificial SEI are the ideal design compared with the insufficient single protective layer. Recently, Zhang et al. demonstrated a dual-layered film constructed on the surface of Li metal anode by spontaneous reaction between Li metal and fluoroethylene carbonate (FEC) solvent.[36] A typical dual-layered structure is afforded on Li metal with compact organic components on the top and rigid inorganic components near the Li surface. The dual-interfacial layer can prevent corrosion from the organic electrolyte and achieve dendrite-free Li deposition. However, the fabrication of dual protective layers with both controllable compositions and thicknesses has been rarely reported due to the highly sensitive physical and chemical properties of Li metal.

Atomic layer deposition (ALD) and molecular layer deposition (MLD) are advanced gas-phase thin-film deposition techniques with excellent coverage and conformal deposition under relatively low temperatures with precise control over coating thickness.[37–40] ALD and MLD have been widely studied in the application of energy storage and conversion.[41–44] Particularly, ALD and MLD are regarded as the ideal approaches to address the surface/interface challenges facing in both liquid-based and solid-state batteries. Meanwhile, ALD and MLD can be used to deposit inorganic films (such as metal oxides) and organic/hybrid film (such polymers), respectively.[45–48] The ALD metal oxide thin films are generally stiff and brittle; on the contrary, the MLD films show higher flexibility. Moreover, the ALD films are much denser compared with MLD films. However, the polymeric MLD films present the porous structure due to the organic chains.[49–51] With the different properties, the dense ALD films are expected to be used to block the electron transport pathway and the reactions between electrolyte and electrodes. The porous MLD films can be used to relieve the volume changes due to the high flexibility.[52,53] In the reported literature, different ALD/MLD films of Al_2O_3, alucone, polyurea, Li_xAl_yS, and LiF have been demonstrated as effective protective layers for Li metal anode with enhanced electrochemical performances. However, the currently developed ALD/MLD films are still insufficient for long-life Li metal anodes. It is believed that the natural SEI-inspired structures with multilayer designs are the ideal artificial SEI for Li metal anodes combining both ALD and MLD techniques. A bilayer consisting of a

[1]Department of Mechanical and Materials Engineering, University of Western Ontario, London, ON N6A 5B9, Canada

[2]General Motors R&D Center, Warren, MI 48090-9055, USA

[3]Department of Physics and Astronomy, University of Western Ontario, London, ON N6A 3K7, Canada

[4]Department of Mechanical and Industrial Engineering, University of Toronto, Toronto M5S 3G8, Canada

[5]These authors contributed equally

[6]Lead Contact

*Correspondence: filleter@mie.utoronto.ca (T.F.), mei.cai@gm.com (M.C.), xsun@eng.uwo.ca (X.S.)

https://doi.org/10.1016/j.matt.2019.06.020

dense ALD inner layer and a porous MLD outer layer could be a promising solution. On one hand, the dense ALD films as inner layers can be used to transport Li^+ while blocking the pathway of electrons and the reactions between electrolyte and Li metals. On the other hand, the highly flexible and porous MLD films are used as an outer shell to provide the channel for electrolyte diffusion and relieve the volume change of Li metals during cycling. However, there is no report on the fabrication of a dual-protective layer for Li metal anode by ALD and MLD techniques. In this case, the combination of ALD and MLD to realize coatings with controllable compositions and thickness is promising for fabrication of an artificial SEI for Li metal anode with rational design.

Herein, we demonstrate the natural SEI-inspired dual protective layer for highly stable Li metal anodes with rationally designed and precisely controlled compositions and thicknesses by ALD and MLD techniques. The sequences of ALD and MLD deposition were used to control the compositions of the dual protective layer, and the thicknesses of the coating were adjusted by the numbers of ALD/MLD cycles. As a result, the dual protective layer with the structure similar to that of naturally formed SEI (an organic outer layer and inorganic inner layer) presents the best electrochemical performances in two types of electrolytes. The thicknesses of both the organic layer and inorganic layer have also been optimized in detail. Surface/interface chemistry analysis indicates that the natural SEI-inspired dual protective layer is very robust after the electrochemical plating/stripping process, and dendrite-reduced Li deposition is achieved with the designed coating. Our design of natural SEI-inspired dual protective layer with a precisely controlled thickness and composition for a highly stable Li metal anode may bring new opportunities for the realization of next-generation high-energy-density Li metal batteries.

RESULTS

Fabrication and Characterization of the Dual Protective Layer by ALD and MLD

Figure 1A shows the schematic diagram of the fabrication process of the dual protective layer by ALD and MLD. In this study, the ALD inorganic Al_2O_3 and MLD organic alucone were used as the typical materials for demonstrating the concept. The sequences of ALD and MLD deposition were used to control the compositions of the dual protective layers. When the MLD organic layer is firstly deposited (as inner layer near Li surface), followed by the deposition of the ALD inorganic layer (as outer layer), the samples are named ALD/MLD/Li. In contrast, when the ALD Al_2O_3 is deposited as an inner layer and MLD alucone is synthesized as an outer layer, the electrodes are noted as MLD/ALD/Li. The thicknesses of dual protective layers were also adjusted by ALD and MLD cycles, in which 5, 25, 50, and 100 cycles of ALD/MLD were deposited for optimization. In this case, different samples of *5ALD/5MLD/Li*, *5MLD/5ALD/Li*, *25ALD/25MLD/Li*, *25MLD/25ALD/Li*, *50ALD/50MLD/Li*, *50MLD/50ALD/Li*, *100ALD/100MLD/Li*, and *100MLD/100ALD/Li* have been fabricated to create a comprehensive study. For example, 50ALD/50MLD/Li means 50 cycles of ALD as the outer layer and 50 cycles of MLD as the inner layer. Inversely, 50MLD/50ALD/Li corresponds to the dual layer of 50 cycles of MLD as outer layer and 50 cycles of ALD as inner layer. The morphologies of the dual-layer protected Li were tested by scanning electron microscopy (SEM), as shown in Figures S1–S3. Note that for all thicknesses of the dual protective layers, the Li foil can maintain the smooth surface without any obvious morphological changes.

The mechanical properties of the ALD/MLD and MLD/ALD dual-layer films were investigated by conducting atomic force microscopy (AFM) film-deflection

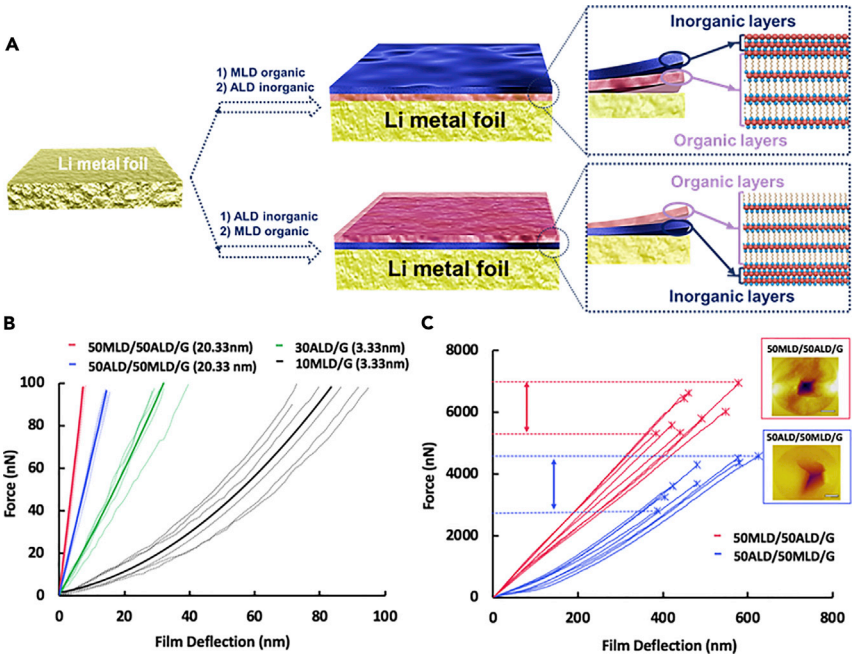

Figure 1. Schematic Diagram and Mechanical Properties of the Dual Protective Layers

(A) Schematic diagram of the fabrication process of the dual protective layer by ALD and MLD.

(B) Force-deflection curve of freestanding films deflected within an elastic regime.

(C) Force-deflection curve of the dual-layer films deflected to failure. Inset: AFM topography images of the failed freestanding dual-layer films. The crosses indicate the failure point. Scale bars, 500 nm.

measurements. To better understand the behavior of ALD/MLD and MLD/ALD films, we also investigated the mechanical properties of individual MLD and ALD films. Four samples consisting of 10 cycles ALD (10ALD), 30 cycles MLD (30MLD), 50MLD/50ALD, and 50MLD/50ALD were deposited over single-layer graphene (used as a supporting layer) on holey transmission electron microscopy grids, and the AFM tip deflected the middle of the suspended films following a previously reported method used for thin films.[54] Prior to elastic deflection, tapping-mode AFM topography imaging was performed to identify damage-free films and also align the AFM diamond tip in the center of the holes covered with film. AFM topography imaging was also performed after elastic deflection to ensure that no damage occurred to the deflected film. The elastic behavior of each film was studied by deflecting the film with a maximum normal force of 100 nN at a constant displacement rate of 10 μms^{-1}. For each sample, at least 15 independent freestanding films were measured. No significant hysteresis, which can otherwise indicate slippage or weak bonding between layers, was observed in the elastic testing regime. The force-deflection curves in Figure 1B show representative elastic behavior of 10ALD/G (3.33 nm), 30MLD/G (3.33 nm), 50ALD/50MLD/G (20.33 nm), and 50MLD/50ALD/G (20.33 nm) films. As expected, the 30MLD/G film exhibits lower stiffness and higher flexibility as compared with the 10ALD/G film of similar thickness (~3 nm). Table S2 shows the stiffness calculated from the slope of elastic force-deflection curves of each film. Both 50MLD/50ALD/G and 50ALD/50MLD/G with a thickness of 20.33 nm exhibited higher stiffness than individual 10ALD/G and 30MLD/G (3.33) films, which is expectable due to the greater thickness. Furthermore, 50MLD/50ALD/G films were found to exhibit higher stiffness than 50ALD/50MLD/G films.

The mechanical behavior of the 50MLD/50ALD/G and 50ALD/50MLD/G films was further investigated by deflecting the films to failure as shown in Figure 1C. At least 15 independent freestanding films were indented to failure for each dual-layer film. For all samples, a sudden decrease in the force was observed (crosses in Figure 1C show failure points) which indicated the failure of the films. AFM topography imaging performed after indentation to failure further confirmed failure of the film, shown as an example in Figure 1C for each dual-layer film. The calculated average failure forces for 50MLD/50ALD/G were found (see Table S2) to be ~50% higher than 50ALD/50MLD/G while the deflection depth at failure was in a similar range, indicating higher strength of the MLD/ALD/G layering configuration. During electrochemical cycling, while both dual-layer films consist of an MLD flexible layer, a combination of the local flexibility of the MLD layer as well as the higher strength of 50MLD/50ALD/G are believed to help the coating suppress crack formation over a higher range of forces in comparison with the 50ALD/50MLD/G films.

To prove the successful demonstration of the dual protective layer concept, we carried out different characterizations to understand the surface and interface compositions. Rutherford backscattering spectrometry (RBS) was performed to probe the composition of the dual-layers and the element depth distributions. Figures S3–S5 show the RBS spectra and simulated depth profiles for the different samples. For example, Figures S4A and S4B display the RBS spectra and simulated depth profiles for 50MLD/50ALD/Li and 50ALD/50MLD/Li, respectively. The presence of Al, C, and O peaks from the surface can confirm the successful synthesis of an Al-containing layer on Li metal. Particularly, C spectra and the depth profiles of 50MLD/50ALD/Li and 50ALD/50MLD/Li present an obvious difference. Similar to the time-of-flight secondary ion mass spectrometry (TOF-SIMS) results, the C spectra show consistent features with the organic linker of ethylene glycol in the MLD alucone layers. For the 50MLD/50ALD/Li (Figure S4A), the content of C is much higher from the outer layer of alucone compared with the inner layer of Al_2O_3. However, the content of C increases from ~0% to 20% from the top surface to the interface near Li for 50ALD/50MLD/Li. Figures S4 and S6 show the RBS spectra and simulated depth profiles for dual layers with different thicknesses (25ALD/25MLD/Li, 25MLD/25ALD/Li, 100ALD/100MLD/Li, and 100MLD/100ALD/Li). The C spectra from all the samples demonstrate the clear edges from the organic layer of alucone and inorganic layer of Al_2O_3. Moreover, the thicknesses of all the samples are simulated from the RBS spectrum, as shown in Table S1. The thicknesses increase from ~15 nm to ~60 nm with an increase in ALD/MLD cycles from 25 cycles to 100 cycles. It is worth noting that the thicknesses of MLD/ALD/Li are always slightly larger than those of the ALD/MLD/Li samples. This observation can be explained by the higher reactivity between H_2O and Li during the deposition process of Al_2O_3 as an inner layer, which was reported previously.[46]

Figures 2A–2D, S7, and S8 show the TOF-SIMS depth profiles and chemical ion images for different samples. In particular, Figures 2A–2D present the TOF-SIMS depth profiles and chemical ion images of Li^-, Al^-, C_2Al^-, AlO_2^-, and C_2OAl^- species for 50MLD/50ALD/Li and 50ALD/50MLD/Li, respectively. From the chemical ion images in both figures, obvious species of C_2Al^-, C_2OAl^- (from organic alucone) and Al^-, AlO_2^- (from both inorganic Al_2O_3 and organic alucone) are observed to identify the deposition of the Al-containing film on Li metal. Moreover, there is almost no signal of Li^- species detected, indicating that the surface of Li metal is completely covered by the ALD/MLD films. It can be seen that the AlO_2^- distributes from top surface to Li surface for both 50MLD/50ALD/Li and 50ALD/50MLD/Li

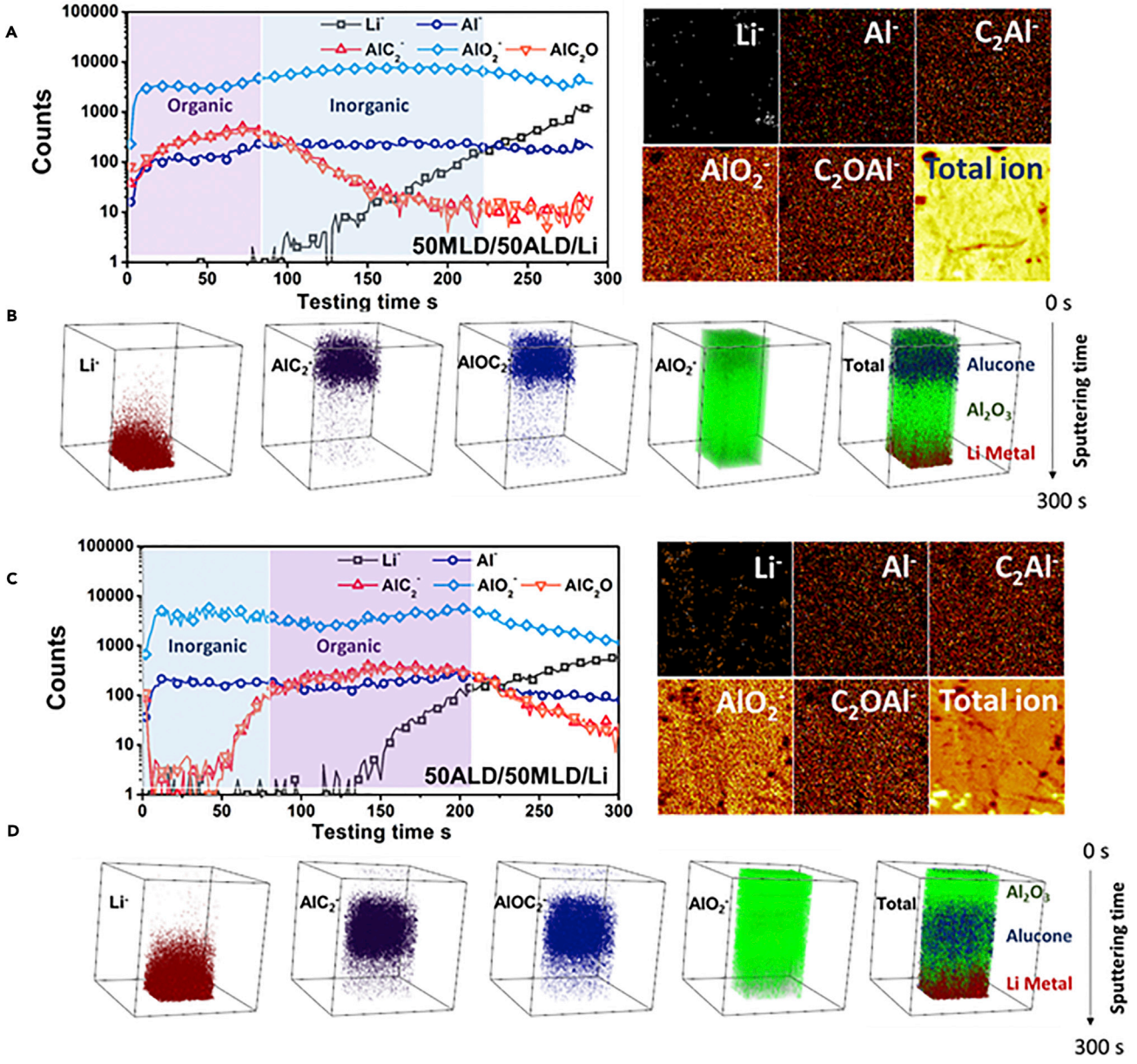

Figure 2. Chemical Compositions of the Dual Protective Layers

(A) TOF-SIMS depth profiles and chemical ion images of the Li^-, Al^-, C_2Al^-, AlO_2^-, and C_2OAl^- species for 50MLD/50ALD/Li.

(B) The 3D view images of the sputtered volume corresponding to the depth profiles in (A) showing the dual protective structure.

(C) TOF-SIMS depth profiles and chemical ion images of the Li^-, Al^-, C_2Al^-, AlO_2^-, and C_2OAl^- species for 50ALD/50MLD/Li.

(D) The 3D view images of the sputtered volume corresponding to the depth profiles in (B) showing the dual protective structure; the analysis area is 400 × 400 μm^2.

because this species can be generated from both ALD Al_2O_3 and MLD alucone (Al-ethylene glycol). Remarkably, the depth profiles of C_2Al^- and C_2OAl^- for 50MLD/50ALD/Li and 50ALD/50MLD/Li exhibit an obvious difference. The C_2Al^- and C_2OAl^- species are the characteristic components from organic alucone film. In Figures 2A and 2B for 50MLD/50ALD/Li, the signals of C_2Al^- and C_2OAl^- keep at 100 counts before ~100 s of sputtering, corresponding to the organic alucone as the outer layer for 50MLD/50ALD/Li. After 100 s of sputtering, the signals of C_2Al^-

and C_2OAl^- significantly decrease into 10 counts, indicating that the inner layer of 50MLD/50ALD/Li is inorganic Al_2O_3. From Figures 2C and 2D of 50ALD/50MLD/Li, the signals of C_2Al^- and C_2OAl^- are relatively low in the outer layer and rise up in the inner layers. The TOF-SIMS results provide strong evidence that the dual-layer design with controllable composition has been successfully fabricated via the combination of ALD and MLD. The TOF-SIMS results of dual layers with different thicknesses (25ALD/25MLD/Li, 25MLD/25ALD/Li, 100ALD/100MLD/Li and 100MLD/100ALD/Li) are presented in Figures S7 and S8. The signals of C_2Al^- and C_2OAl^- show a similar trend with Figures 2A–2D, indicating the controllable compositions by changing the sequence of ALD and MLD depositions. Meanwhile, the increase in sputtering times to reach the bulk Li demonstrates the increase in thicknesses with the ALD/MLD cycles from 25 to 100. As confirmed by RBS and TOF-SIMS analysis, the dual protective layers with controllable compositions and thicknesses were successfully fabricated by controlling the sequences and cycles of ALD and MLD during the deposition process. It should be emphasized that only gas-phase deposition techniques of ALD and MLD can realize the highly controlled stoichiometric composition and thickness into the atomic level on the Li metal anode.

Electrochemical Performances of the Dual Protective Layer by ALD and MLD

Symmetrical cells were assembled to evaluate the Li plating/stripping behavior of the dual protective layer for Li electrodes. Two popular types of electrolytes were used to demonstrate the universal applicability of the dual protective layer. Figures 3A and 3B show the cycling stability of pristine Li foil, 50ALD/50MLD/Li, and 50MLD/50ALD/Li in carbonate-based electrolyte (1 M $LiPF_6$ in ethylene carbonate [EC]/diethyl carbonate [DEC]/dimethyl carbonate [DMC] of 1:1:1 volume ratio with 10% FEC). In Figure 3A, with the current density of 1 mA cm^{-2} and capacity of 1 mAh cm^{-2}, the initial Li stripping/plating overpotential of pristine Li foil is approximately 50 mV (versus Li^+/Li) and rapidly increases to over 500 mV (versus Li^+/Li) after ~300 h. Subsequently, the overpotential of the pristine Li foil suddenly drops to ~20 mV, indicating the occurrence of a short-circuit in the cell. However, the dual protective layer of 50ALD/50MLD/Li displays significant improvement on the cycling stability. The overpotential of 50ALD/50MLD/Li starts to increase after ~700 h of cycling with large polarization in the voltage profiles. More promising, the 50MLD/50ALD/Li presents the most stable performances with a cycling life of over 850 h without any short-circuit. Figure 3B shows the performances of Li/Li symmetric cells with a higher capacity of 2 mAh cm^{-2}. The pristine Li foil still shows the increased overpotential and subsequent short-circuit after ~350 h. In comparison, the 50ALD/50MLD/Li displays improved stability with a stable overpotential over 600 h. Remarkably, the 50MLD/50ALD/Li still presents the best stability among these sample with low overpotential of ~130 mV over 700 h. For comparison, the symmetric cell performances of single protective layers of 50ALD/Li and 50 MLD/Li are shown in Figure S9. Consistent with our previous work, 50MLD/Li exhibits a better performance than that of 50ALD/Li and pristine Li foil due to the high flexibility of MLD films. However, the single protective layers of either ALD or MLD are still inferior to the dual protective layers.

Figures 3C and 3D present the cycling stability of pristine Li foil, 50ALD/50MLD/Li, and 50MLD/50ALD/Li in ether-based electrolyte (1 M LiTFSI in dioxolane [DOL]/dimethoxyethane [DME] of 1:1 volume ratio). At the high current density of 5 mA cm^{-2} in the ether-based electrolyte, the short-circuit happens for pristine Li foils after only 340 h, in which the overpotential of it suddenly drops to ~10 mV. The sudden voltage drop can be explained by the serious dendrite growth on the Li surface with penetration through the separator. Promisingly, both of the dual

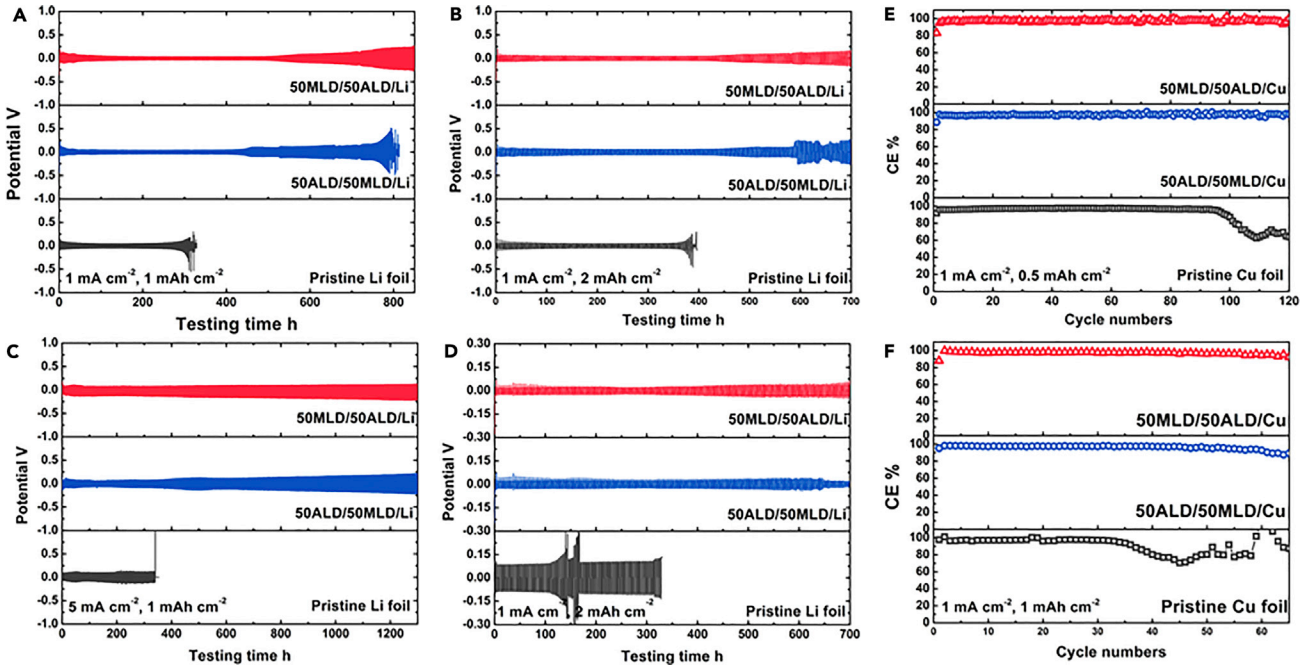

Figure 3. Electrochemical Performance of Dual Protective Layer for Li Electrode

(A and B) The overpotential of Li/Li symmetric cells using pristine Li foil, 50ALD/50MLD/Li, and 50MLD/50ALD/Li in carbonate-based electrolyte: (A) current 1 mA cm^{-2}, capacity 1 mAh cm^{-2}; (B) current 1 mA cm^{-2}, capacity 2 mAh cm^{-2}.

(C–F) Overpotential of Li/Li symmetric cells using pristine Li foil, 50ALD/50MLD/Li, and 50MLD/50ALD/Li in ether-based electrolyte: (C) current 5 mA cm^{-2}, capacity 1 mAh cm^{-2}; (D) current 1 mA cm^{-2}, capacity 2 mAh cm^{-2}. CE evolution of Li plating/stripping on the bare Cu, 50ALD/50MLD/Cu, and 50MLD/50ALD/Cu: (E) current 1 mA cm^{-2}, capacity: 0.5 mA cm^{-2}; (F) current 1 mA cm^{-2}, capacity 1 mAh cm^{-2}.

protective layer-coated Li electrodes (50ALD/50MLD/Li and 50MLD/50ALD/Li) display superior stable electrochemical plating/stripping performance for over 1,300 h, which is almost 4-fold higher than that of the pristine Li anode. Moreover, the overpotential of 50MLD/50ALD/Li after 1,300 h of cycles is slightly lower than that of the 50ALD/50MLD/Li, indicating smaller polarization with the organic MLD layer as outer layers. When increasing the capacity to 2 mAh cm^{-2} and keeping the current density at 1 mA cm^{-2}, the pristine Li electrode shows even worse performances with increasing polarizations after only ~150 h. For the 50ALD/50MLD/Li, the performance can be stabilized for over 600 h and with cell failure after 650 h. Furthermore, the 50MLD/50ALD/Li possesses stable performances for over 700 h with small polarizations.

In comparison, the electrochemical performances in the symmetrical cells of single protective layers of 50ALD/Li and 50 MLD/Li are shown in Figure S10. At the different current densities and capacities, the single protective layers of 50ALD/Li and 50 MLD/Li can improve the lifetime compared with pristine Li, in which the organic MLD coating demonstrates better stability than the inorganic ALD coating. However, the performances with single protective layers are still not as stable as the dual protective layers for Li electrodes. The electrochemical results of the symmetric cells with both carbonate-based and ether-based electrolyte reveal that the dual protective layer demonstrates significantly enhanced electrochemical performance compared with pristine Li foil and the single protective layer of either ALD or MLD. Interestingly, the compositions of the dual protective layer also slightly affect the stability of the symmetric cells, in which the 50MLD/50ALD/Li display the most stable performances with the longest lifespan and lowest overpotential.

Furthermore, the Li plating/stripping CE has also been evaluated using Cu foil and dual-layer coated Cu foil as current collectors. Similar dual protective layers are deposited on Cu foil with the controlled ALD and MLD sequence, named 50ALD/50MLD/Cu and 50MLD/50ALD/Cu, respectively. Figures 3E and 3F shows the CE evolution of pristine Cu foil, 50ALD/50MLD/Cu, and 50MLD/50ALD/Cu under different testing conditions. A fixed amount of Li (0.5 mAh cm^{-2} or 1 mAh cm^{-2}) is plated on the Cu, followed by stripping at the same current up to 1 V (versus Li^+/Li). The CE of each cycle is calculated by the amount of stripped Li divided by the amount of plated Li. At the current density of 1 mA cm^{-2} and the capacity of 0.5 mAh cm^{-2}, the pristine CE of Cu foil degrades significantly to 60% after 100 cycles. In contrast, the Cu foils with dual protective layers provide an average CE of over ~97.5% after 120 cycles. When increasing the capacity into 1 mAh cm^{-2}, the average CE of 50ALD/50MLD/Cu and 50MLD/50ALD/Cu between 45 and 65 cycles are 94.2% and 96.1%, respectively. However, the CE of pristine Cu foil starts to decrease after only 30 cycles.

Besides the precisely regulated composition of the dual protective layer, the thicknesses of the films were also controlled by ALD and MLD. As discussed above, the dual protective layers on Li electrodes with different thicknesses have been successfully fabricated, which are confirmed by TOF-SIMS and RBS techniques. The electrochemical performances of the dual protective layers with different thicknesses were optimized in detail, as shown in Figures S11–S13. Figure S11 presents the cycling stability of 25ALD/25MLD/Li, 25MLD/25ALD/Li, 100ALD/100MLD/Li, and 100MLD/100ALD/Li in carbonate-based electrolyte with a current density of 1 mA cm^{-2} and a capacity of 1 mAh cm^{-2}. Figure S12 shows the cycling stability of 25ALD/25MLD/Li, 25MLD/25ALD/Li, 100ALD/100MLD/Li, and 100MLD/100ALD/Li in ether-based electrolyte with the current density of 5 mA cm^{-2} and a capacity of 1 mAh cm^{-2}. It can be observed that the optimized thicknesses of dual-protective layers are between 25/25 cycles and 50/50 cycles in both types of the electrolytes. From Figure S13, the average CE of 25ALD/25MLD/Li, 25MLD/25ALD/Li, 100ALD/100MLD/Li, and 100MLD/100ALD/Li between 65 cycles to 120 cycles are 73.9%, 94.7%, 95.1%, and 94.0%, respectively.

To further demonstrate the unique properties of the dual protective layer, we investigated different full-cell systems using pristine Li and dual-layer protected Li electrodes as the anode. Based on the symmetric cell performances discussed above, the 50MLD/50ALD/Li electrode is used as an example for the full cells. The Li-S coin cells are assembled with C/S composites as a cathode electrode in the ether-based electrolyte (1 M LiTFSI in DOL/DME with 5% $LiNO_3$) at a current density of 700 mA g^{-1} with sulfur loading of ~2.0 mg cm^{-2}. The long-term cycling performance of these cells is shown in Figure 4A. For the pristine Li electrode, the obvious capacity fade of C/S cathode can be observed after 200 cycles due to the self-propagating reaction since the dissolved polysulfides enable to react with Li metal and finally form insulated Li_2S deposited on Li foil. After 350 cycles, the capacity of the cell remains only 236.9 mAh g^{-1}. It is very promising that with a designed dual protective layer, the cell using 50MLD/50ALD/Li as an anode electrode is more stable and the reversible capacities have been significantly improved after 350 cycles, which is 711.4 mAh g^{-1}. The discharge-charge profiles of pristine Li and 50MLD/50ALD/Li after the 50th, 150th, 250th, and 350th cycles are shown in Figure 4A. Impressively, the Li-S battery using dual-layer protection demonstrates stable, flat, and highly reversible discharge-charge potential plateaus, while the potential plateaus of the Li-S cell using pristine Li foil gradually decay during cycling. The cycling

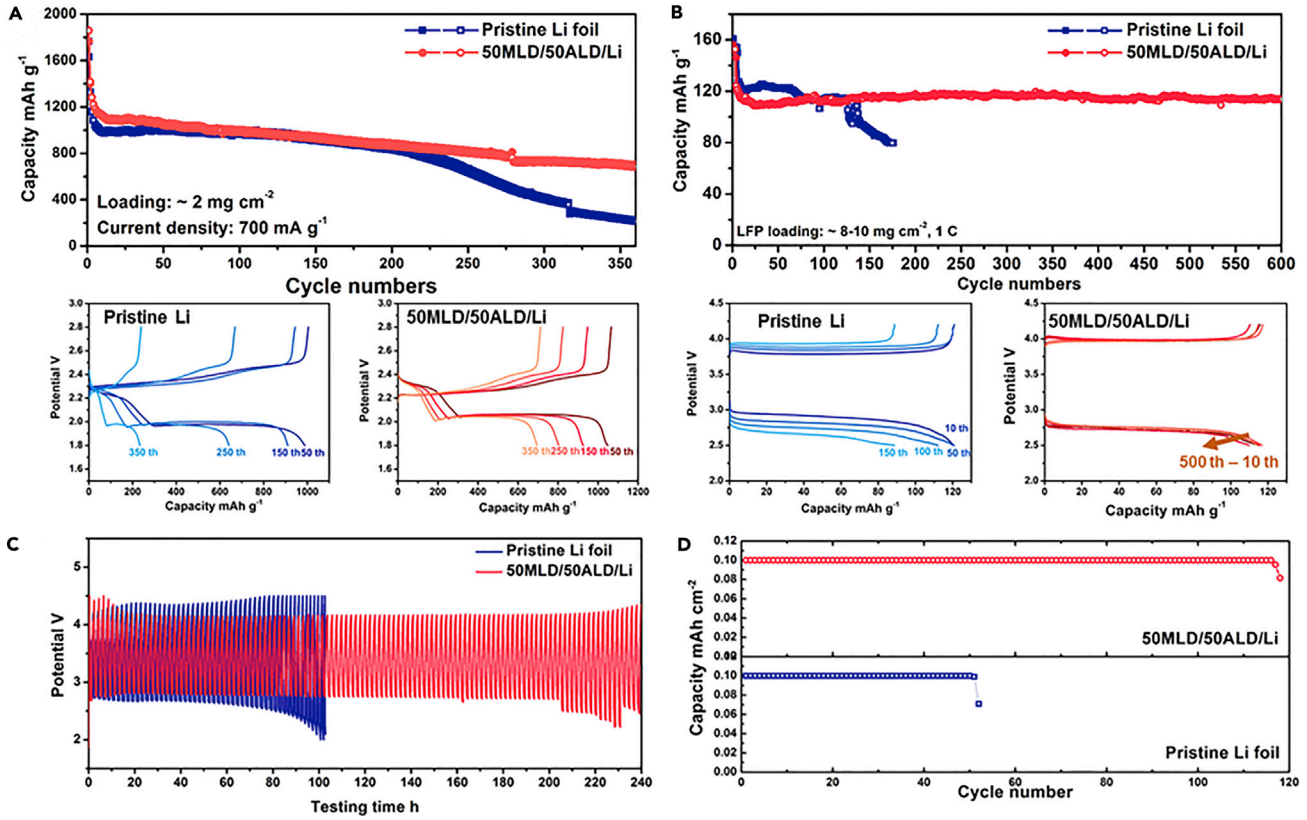

Figure 4. Full-Cell Performances Using Pristine Li Foil and Dual-Layer Protected Li Electrode

(A) Cycling performance and voltage hysteresis profiles of Li-S full cells (C/S as cathode) using pristine Li foil and 50MLD/50ALD/Li as anode electrode.

(B) Cycling performance and voltage hysteresis profiles of full cells (C/$LiFePO_4$ as cathode) using pristine Li foil and 50MLD/50ALD/Li as anode electrode at 1 C (1 C = 170 mA g^{-1}).

(C and D) Voltage hysteresis profiles (C) and cycling performances (D) of Li-O_2 full cells (CP-NCNTs as cathode) using pristine Li foil and 50MLD/50ALD/Li as anode electrode at the current density of 0.1 mA cm^{-2}.

performance of another repeatable Li-S full cell is shown in Figure S14. After 350 cycles, the reversible capacities of the cell using pristine Li foil and 50MLD/50ALD/Li are 172.5 and 686.7 mAh g^{-1}, respectively. The results highly confirm that the designed dual protective layer can significantly increase the long lifetime of the Li anode and improve the utilization of the sulfur by prevention of the corrosion and side reactions between Li and polysulfides.

Other Li metal batteries using $LiFePO_4$ (LFP) as cathodes have also been demonstrated, shown in Figure 4B. The LFP cells were firstly activated at 0.1 C for 3 cycles and then cycled at 1 C for long-term cycling performance. In the cell using pristine Li foil, the discharge/charge capacity starts fading after 150 cycles, decreasing to about 80 mAh g^{-1} after 160 cycles. However, using 50MLD/50ALD/Li as the anode electrode, the cell maintains an extremely stable capacity of ~114.0 mAh g^{-1} after 600 cycles.

In addition, the electrochemical performances of the Li-O_2 cells have also been performed by using 2016-type coin cells of a carbon-based cathode (N-doped carbon nanotube grown on carbon paper, NCNTs-CP), an electrolyte of $LiCl_4$ in tetraethylene glycol dimethyl ether (TEGDME), and a pristine Li foil or protected Li foil (50MLD/50ALD/Li) as the anodes. Figures 4C and 4D present the charge-discharge

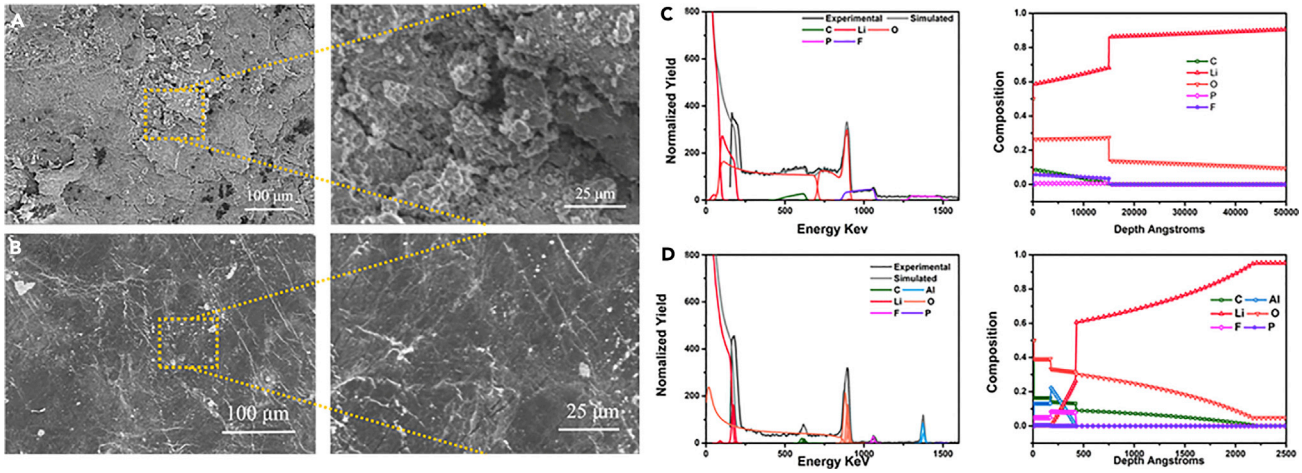

Figure 5. Surface Characterization of Dual Protective Layer after Cycling

Top-view SEM images of (A) pristine Li foil and (B) 50MLD/50ALD/Li after electrochemical cycling; RBS spectra and calculated depth profiles (based on RBS results) of (C) pristine Li foil and (D) 50MLD/50ALD/Li after cycling.

profiles and cycling performances of the Li-O_2 cells using pristine Li foil and 50MLD/50ALD/Li as anode electrodes, respectively. It can be observed that the Li-O_2 cell with 50MLD/50ALD/Li anode can be cycled 110 cycles with no capacity loss, which is two times higher than that of the cell using pristine Li foils. The results reveal that the dual protective layer of 50MLD/50ALD can effectively reduce the degradation of Li anodes against O_2 corrosion and Li dendrite formation. The electrochemical performances tested in both symmetric cell and Li metal full cell demonstrate that the rationally designed dual protective layer can significantly improve the stability of Li metal anode in different systems and shows potential for the use in next-generation Li metal batteries.

Unveiling the Enhancing Mechanism via Surface Characterizations of Dual Protective Layer after Cycling

To understand the influence of the dual protective layers on suppressing Li dendrite growth, we imaged the morphology of Li metal after cycling by SEM. Similarly, the 50MLD/50ALD/Li is used as an example to demonstrate the surface changes. Figure S15 shows the SEM images of pristine Li foil after the different depth of electrochemical cycling (10 cycles, 20 cycles, and 30 cycles) in carbonate-based electrolyte at a current density of 1 mA cm^{-2} with a capacity limit of 1 mAh cm^{-2}. Although the additive of FEC can effectively reduce the dendrite formation during the Li deposition for pristine Li foil, the serious mossy-like Li and "dead Li" layer are still formed during cycling. With a deeper cycling to 50 electrochemical plating/stripping cycles (Figure 5A) a rougher surface is obtained, and obvious cracks are observed on the Li. These issues are the direct cause of the increasing polarization of the cell and, finally, the short-circuit. In comparison, the morphology of the cycled Li with dual protective layers is drastically different. Figures S16 and 5B show the SEM images of 50MLD/50ALD/Li after various electrochemical cycles of 10, 20, 30, and 50 cycles under the same testing condition. Compared with the SEM images before cycling (Figure S2), there are no significant changes in the morphologies with different electrochemical cycles. This result indicates that the protective films are robust during the plating/stripping process and the mossy Li growths and dead Li formations are effectively suppressed with coating. The Li-deposition morphologies in the ether-based electrolyte are

also observed, as shown in Figures S17 and S18. Figure S17 presents the SEM images of pristine Li foil after 10 cycles and 50 cycles electrochemical deposition process in the ether-based electrolyte at a current density of 5 mA cm^{-2} with a capacity of 1 mAh cm^{-2}. A rough surface with mossy Li growth is observed after 10 cycles, and large cracks with 20 μm width are formed after several cycles. However, with dual protective layers, the surface of the Li electrodes after cycling is much smoother and both dendritic and mossy Li are significantly suppressed, as seen in Figure S18.

SEI compositions are another key factor in understanding the Li-deposition behavior. To elucidate compositional changes following the plating/stripping cycling experiments, we performed RBS and TOF-SIMS measurements. Figure S19 presents the RBS spectra of pristine Li foil and 50MLD/50ALD/Li after 10 cycles of electrochemical plating/stripping in the carbonate-based electrolyte at a current density of 1 mA cm^{-2} with a capacity limit of 1 mAh cm^{-2}. The corresponding calculated depth profiles of pristine Li foil and 50MLD/50ALD/Li after cycling are shown in Figures 5C and 5D, respectively. From the depth profiles for pristine Li foil, there is serious penetration of P and F from the electrolyte into a subsurface layer, as well as oxidation. The thickness of the P- and F-containing layer is around 1.5 μm and the oxidation layer is over 5 μm. Remarkably, P and F only are localized in the first 40 nm of the top surface layer. When comparing the RBS depth profiles before and after cycling, both of the composition and thickness of the dual protective layer (50MLD/50ALD) change very little, indicating that the films act as good protective barriers. Figures 6A and 6B present the SIMS depth profiles of pristine Li foil and 50MLD/50ALD/Li after 30 cycles of plating/stripping cycling experiments at a current density of 1 mA cm^{-2} with a capacity limit of 1 mAh cm^{-2}, respectively. Similarly, while the pristine Li shows significant penetration of F from electrolyte with long sputtering time (over 1,000 s), the signal of F^- species drastically decreases in the first 100 s of sputtering. Meanwhile, the feature species of C_2Al^-, AlO_2^-, and C_2OAl^- from the dual protective layer remain on the top surface and with only small changes compared with the spectra before cycling. Figures S21A and 6C presents the 3D view images of the sputtered volume corresponding to the depth profiles of pristine Li foil and 50MLD/50ALD/Li after cycling in carbonate-based electrolyte. It can be clearly seen that the F^- penetrate from the top surface to the end of sputtering areas. Promisingly, the C_2OAl^- species remain as a protective layer on the surface of Li and the penetration of F is suppressed. To further understand the interface, we performed electrochemical impedance spectroscopy (EIS) before cycling and after 100 cycles, as shown in Figures S22A and S22B. Figure S22A presents the initial spectra with an obvious increase in the impedance for the 50MLD/50ALD/Li compared with pristine Li foil before cycling. The larger resistance of 50MLD/50ALD/Li is attributed to the non-ionic conductive films of Al_2O_3 and alucone before lithiation. After 100 cycles of plating/stripping process (Figure S22B), the R_{SEI} of both bare Li and 50MLD/50ALD/Li decreases, in which the resistance of 50MLD/50ALD/Li is lower than pristine Li foil. The decreasing of the R_{SEI} for 50MLD/50ALD/Li indicates the lithiation of the dual protective layers with robust properties. The consistent results from RBS, TOF-SIMS, and EIS indicate that the dual protective films are very robust and can retain their structures after electrochemical cycling.

Meanwhile, the two electrodes of pristine Li foil and 50MLD/50ALD/Li were also cycled in the ether-based electrolyte to analyze the surface compositions. Figures S20, 6D, and 6E show the RBS result and TOF-SIMS depth profiles for pristine Li foil and 50MLD/50ALD/Li in the ether-based electrolyte. Figures S21B and 6F

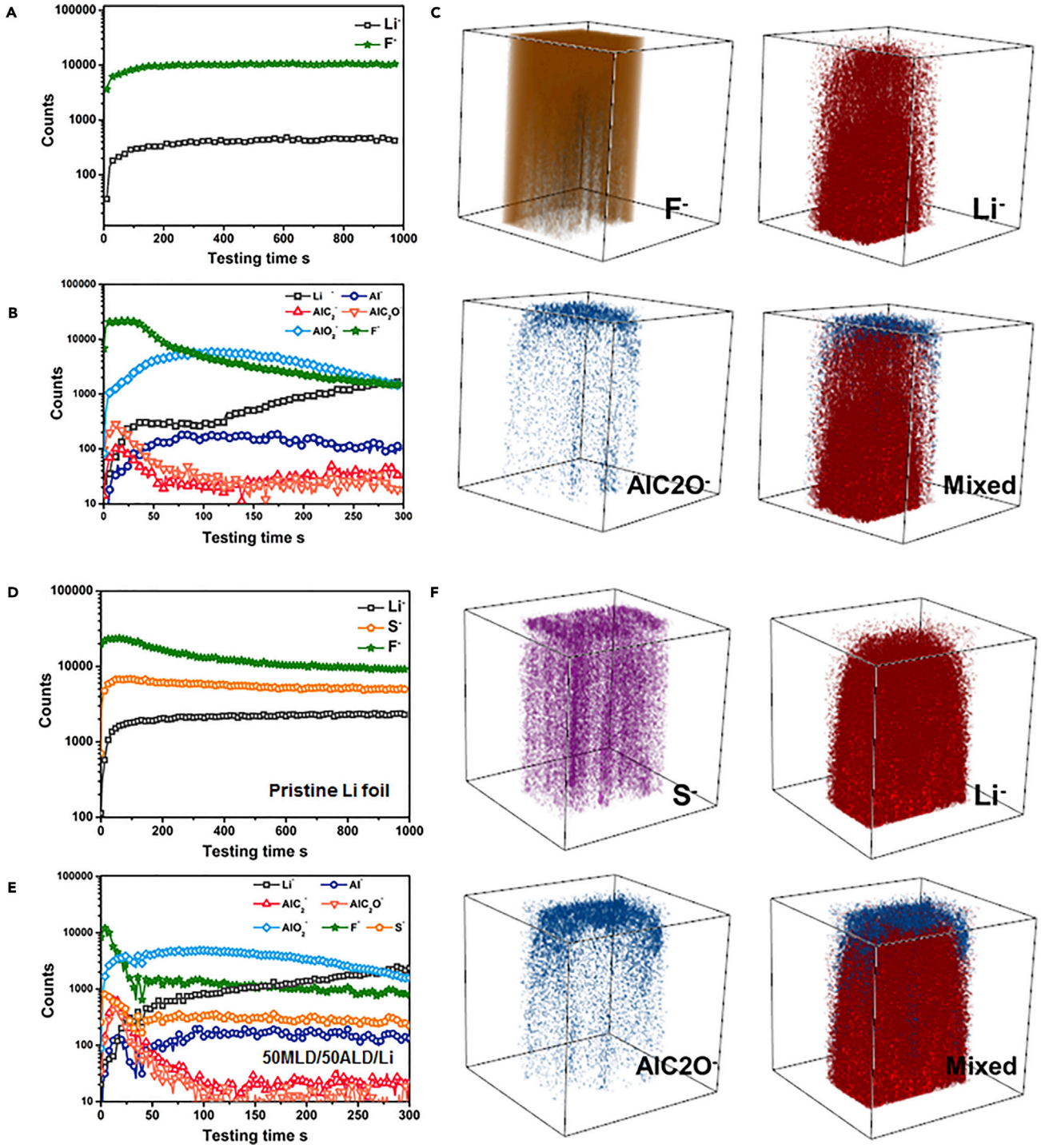

Figure 6. SEI Composition of Dual Protective Layer after Cycling

TOF-SIMS depth profiles of (A and D) pristine Li foil and (B and E) 50MLD/50ALD/Li after cycling. (C) and (F) are the 3D-view images of the sputtered volume corresponding to the depth profiles in (B) and (E) of 50MLD/50ALD/Li after cycling, respectively. The electrochemical testing in (A) to (C) and (D) to (F) are carried out in the carbonate-based electrolyte and ether-based electrolyte, respectively.

presents the 3D view images of the sputtered volume corresponding to the depth profiles of pristine Li foil and 50MLD/50ALD/Li after cycling in ether-based electrolyte. RBS depth profiles show that the penetration/diffusion of F and S is very deep

(5 μm), while the high concentrations of F and S are only contained in the dual protective layer of 40 nm. Meanwhile, the signal of F^- and S^- species from TOS-SIMS depth profiles and related 3D view images keep steady and high over 1,000 s sputtering time. However, both F^- and S^- species significantly decrease in the first 50 s. Moreover, both of the RBS and TOF-SIMS results indicate that the thickness and compositions of the 50MLD/50ALD layer on Li are stable in the ether-based electrolyte.

DISCUSSION

In conclusion, we demonstrate the rational design of a highly controllable natural SEI-inspired dual protective layer for Li metal anodes. First, both the compositions and thicknesses of the dual protective layer can be precisely controlled due to the unique properties of ALD and MLD techniques. We realize the concept of the dual protective layer with different sequences of an organic and inorganic layer on Li metal anode, which is difficult to achieve by other techniques. Second, the symmetrical cells results reveal that the dual protective layer presents much better electrochemical performances than that of the pristine Li electrode and the single protective layer (either ALD or MLD) in both carbonate-based and ether-based electrolytes. Meanwhile, the compositions and thicknesses of the dual layers are optimized in detail, in which the design of the organic layer as the outer layer and inorganic layer as inner layer shows the most stable performances. Third, the full cells, including Li-S and Li-LFP batteries, demonstrate that the optimized dual protective layer of 50MLD/50ALD can significantly enhance the cycling stability and extend the life in both batteries. The cells using 50MLD/50ALD/Li as the anode electrode can deliver the reversible capacities of 711.4 mAh g^{-1} after 350 cycles for Li-S batteries and 114.0 mAh g^{-1} after 600 cycles for Li-LFP batteries. Finally, the surface characterizations, including the morphologies and SEI compositions, as well as the mechanical properties of the layers, have been comprehensively analyzed. The dual protective layer of 50MLD/50ALD can effectively suppress the dendrite growth and dead Li formation. Moreover, the serious penetrations of P and F (or S) are significantly prevented. The dual protective layer is robust during electrochemical plating/stripping, whereby the compositions and thicknesses are retained. Inspired from the naturally formed SEI, the structure of our SEI-like dual-protective layers could be an ideal design as artificial SEI layers. The inorganic ALD Al_2O_3 is deposited as inner layers with dense structure, which can block the reactions between liquid electrolyte and Li metals and limit the pathway of electrons. Meanwhile, the organic MLD alucone film is used as outer layers with porous structure and high flexibility, which can provide the channel for electrolyte diffusion and relive the volume change of Li metals during cycling. Moreover, both of ALD Al_2O_3 and MLD alucone are highly chemically and electrochemically stable during cycling and also could be lithiated in the liquid electrolytes. It is considered that the SEI-like dual-protective layers with ALD as inner layer and MLD as outer layer could be an ideal design. On one hand, the dense ALD films as inner layers can be used to transport Li^+ while blocking the pathway of electrons and the reactions between electrolyte and Li metals. On the other hand, the highly flexible and porous MLD films are used as an outer shell to provide the channel for electrolyte diffusion and relieve the volume change of Li metals during cycling. It is believed that our design of the SEI-like dual-layer protected Li metal anode by ALD and MLD may open up new opportunities for the realization of the next-generation high-energy-density Li metal batteries.

EXPERIMENTAL PROCEDURES

Full details of all experimental procedures are provided in Supplemental Information.

SUPPLEMENTAL INFORMATION

Supplemental Information can be found online at https://doi.org/10.1016/j.matt.2019.06.020.

ACKNOWLEDGMENTS

This research was supported by the Natural Sciences and Engineering Research Council of Canada of Canada (NSERC), the Canada Research Chair Program, the Canada Foundation for Innovation (CFI), General Motors R&D Center, Ontario Research Foundation, and the University of Western Ontario. T.F. acknowledges funding by The Ontario Ministry of Research, Innovation Early Researcher, the Erwin Edward Hart Professorship, NSERC and CFI. We gratefully acknowledge Dr. Heng-Yong Nie for his help in the discussion on TOF-SIMS results. We would like to acknowledge the technical expertise of Mr. Jack Hendriks at Western Tandetron accelerator facility.

AUTHOR CONTRIBUTIONS

Y.Z. and M.A. contributed equally to this work. X.S. and M.C. conceived the overall project; Y.Z. designed the procedure with help from Q.S. and performed the experiments and data analysis, and wrote the manuscript; M.A. and T.F. carried out and analyzed the mechanical properties and wrote the relevant part; C.Z. performed the Li-O_2 full-cell testing; A.C. and L.V.G. helped to carry out the RBS measurements and simulation; C.W. and K.A. helped to perform the LFP full-cell testing; X.L. and F.Z. helped to perform the Li-S full-cell testing; X.Y. and R.L. interpreted the results and data analysis. All authors read and commented on the manuscript.

DECLARATION OF INTERESTS

The authors declare no competing interests.

Received: February 14, 2019
Revised: May 3, 2019
Accepted: June 18, 2019
Published: September 11, 2019

REFERENCES

1. Cheng, X.B., Zhang, R., Zhao, C.Z., and Zhang, Q. (2017). Toward safe lithium metal anode in rechargeable batteries: a review. Chem. Rev. *117*, 10403–10473.

2. Lin, D., Liu, Y., and Cui, Y. (2017). Reviving the lithium metal anode for high-energy batteries. Nat. Nanotechnol. *12*, 194–206.

3. Tikekar, M.D., Choudhury, S., Tu, Z., and Archer, L.A. (2016). Design principles for electrolytes and interfaces for stable lithium-metal batteries. Nat. Energy *1*, 16114.

4. Lu, J., Chen, Z., Pan, F., Cui, Y., and Amine, K. (2018). High-performance anode materials for rechargeable lithium-ion batteries. Electrochem. Energy Rev. *1*, 35–53.

5. Zhang, W., Zhuang, H.L., Fan, L., Gao, L., and Lu, Y. (2018). A "cation-anion regulation" synergistic anode host for dendrite-free lithium metal batteries. Sci. Adv. *4*, eaar4410.

6. Xin, S., You, Y., Wang, S., Gao, H.C., Yin, Y.X., and Guo, Y.G. (2017). Solid-state lithium metal batteries promoted by nanotechnology: progress and prospects. ACS Energy Lett. *2*, 1385–1394.

7. Tan, S.J., Zeng, X.-X., Ma, Q., Wu, X.W., and Guo, Y.G. (2018). Recent advancements in polymer-based composite electrolytes for rechargeable lithium batteries. Electrochem. Energy Rev. *1*, 113–138.

8. Lin, D., Liu, Y., Liang, Z., Lee, H.W., Sun, J., Wang, H., Yan, K., Xie, J., and Cui, Y. (2016). Layered reduced graphene oxide with nanoscale interlayer gaps as a stable host for lithium metal anodes. Nat. Nanotechnol. *11*, 626–632.

9. Liu, Y., Lin, D., Liang, Z., Zhao, J., Yan, K., and Cui, Y. (2016). Lithium-coated polymeric matrix as a minimum volume-change and dendrite-free lithium metal anode. Nat. Commun. *7*, 10992.

10. Zhao, Y., Sun, Q., Li, X., Wang, C., Sun, Y., Adair, K., Li, R., and Sun, X. (2018). Carbon paper interlayers: a universal and effective approach for highly stable Li metal anodes. Nano Energy *43*, 368–375.

11. Zhao, Y., Yang, X., Sun, Q., Gao, X., Lin, X., Wang, C., Zhao, F., Sun, Y., Adair, K., Li, R., et al. (2018). Dendrite-free and minimum volume change Li metal anode achieved by three-dimensional artificial interlayers. Energy Storage Mater. *15*, 415–421.

12. Wood, K.N., Noked, M., and Dasgupta, N.P. (2017). Lithium metal anodes: toward an improved understanding of coupled morphological, electrochemical, and mechanical behavior. ACS Energy Lett. *2*, 664–672.

13. Kim, M.S., Ryu, J.-H., Deepika, Lim, Y., Nah, I., Lee, K.-R., Archer, L.A., and Cho, W. (2018). Langmuir-Blodgett artificial solid-electrolyte interphases for practical lithium metal batteries. Nat. Energy *3*, 889–898.

14. Yang, X., Li, X., Adair, K., Zhang, H., and Sun, X. (2018). Structural design of lithium-sulfur batteries: from fundamental research to practical application. Electrochem. Energy Rev. *1*, 239–293.

15. Xu, W., Wang, J., Ding, F., Chen, X., Nasybulin, E., Zhang, Y., and Zhang, J.-G. (2014). Lithium metal anodes for rechargeable batteries. Energy Environ. Sci. *7*, 513–537.

16. Liu, Y., Lin, D., Jin, Y., Liu, K., Tao, X., Zhang, Q., Zhang, X., and Cui, Y. (2017). Transforming from planar to three-dimensional lithium with flowable interphase for solid lithium metal batteries. Sci. Adv. *3*, eaao0713.

17. Ma, L., Kim, M.S., and Archer, L.A. (2017). Stable artificial solid electrolyte interphases for lithium batteries. Chem. Mater. *29*, 4181–4189.

18. Gu, Y., Wang, W.W., Li, Y.J., Wu, Q.H., Tang, S., Yan, J.W., Zheng, M.S., Wu, D.Y., Fan, C.H., Hu, W.Q., et al. (2018). Designable ultra-smooth ultra-thin solid-electrolyte interphases of three alkali metal anodes. Nat. Commun. *9*, 1339.

19. Pang, Q., Zhou, L., and Nazar, L.F. (2018). Elastic and Li-ion-percolating hybrid membrane stabilizes Li metal plating. Proc. Natl. Acad. Sci. U S A *115*, 12389–12394.

20. Liao, K., Wu, S., Mu, X., Lu, Q., Han, M., He, P., Shao, Z., and Zhou, H. (2018). Developing a "water-defendable" and "dendrite-free" lithium-metal anode using a simple and promising $GeCl_4$ pretreatment method. Adv. Mater. *30*, 1705711.

21. Xie, J., Liao, L., Gong, Y., Li, Y., Shi, F., Pei, A., Sun, J., Zhang, R., Kong, B., Subbaraman, R., et al. (2017). Stitching h-BN by atomic layer deposition of LiF as a stable interface for lithium metal anode. Sci. Adv. *3*, eaao3170.

22. Yan, C., Cheng, X.B., Yao, Y.X., Shen, X., Li, B.Q., Li, W.J., Zhangm, R., Huang, J.Q., Li, H., and Zhang, Q. (2018). An armored mixed conductor interphase on a dendrite-free lithium-metal anode. Adv. Mater. *30*, 1804461.

23. Wei, S., Choudhury, S., Tu, Z., Zhang, K., and Archer, L.A. (2018). Electrochemical interphases for high-energy storage using reactive metal anodes. Acc. Chem. Res. *51*, 80–88.

24. Kozen, A., Lin, C., Pearse, A., Schroeder, M., Han, X., Hu, L., Lee, S., Rubloff, G., and Noked, M. (2015). Next-generation lithium metal anode engineering via atomic layer deposition. ACS Nano *9*, 5884–5892.

25. Kazyak, E., Wood, K.N., and Dasgupta, N.P. (2015). Improved cycle life and stability of lithium metal anodes through ultrathin atomic layer deposition surface treatments. Chem. Mater. *27*, 6457–6462.

26. Cha, E., Patel, M.D., Park, J., Hwang, J., Prasad, V., Cho, K., and Choi, W. (2018). 2D MoS_2 as an efficient protective layer for lithium metal anodes in high-performance Li-S batteries. Nat. Nanotechnol. *13*, 337–344.

27. Yan, J., Yu, J., and Ding, B. (2018). Mixed ionic and electronic conductor for Li-metal anode protection. Adv. Mater. *30*, 1705105.

28. Li, N.W., Yin, Y.X., Yang, C.P., and Guo, Y.G. (2016). An artificial solid electrolyte interphase layer for stable lithium metal anodes. Adv. Mater. *28*, 1853–1858.

29. Liu, B., Gong, Y., Fu, K., Han, X., Yao, Y., Pastel, G., Yang, C., Xie, H., Wachsman, E., and Hu, L. (2017). Garnet solid electrolyte protected Li-metal batteries. ACS Appl. Mater. Interfaces *9*, 18809–18815.

30. Zhao, Y., Goncharova, L., Sun, Q., Li, X., Lushington, A., Wang, B., Li, R., Dai, F., Cai, M., and Sun, X. (2018). Robust metallic lithium anode protection by the molecular-layer-deposition technique. Small Methods *2*, 1700417.

31. Chen, L., Huang, Z., Shahbazian-Yassar, R., Libera, O.A., Klavetter, K.C., Zavadil, K.R., and Elam, J.W. (2018). Directly formed alucone on lithium metal for high-performance Li batteries and Li-S batteries with high sulfur mass loading. ACS Appl. Mater. Interfaces *10*, 7043–7051.

32. Gao, Y., Yan, Z., Gray, J., He, X., Wang, D., Chen, T., Huang, Q., Li, Y., Wang, H., Kim, S., et al. (2019). Polymer-inorganic solid-electrolyte interphase for stable lithium metal batteries under lean electrolyte conditions. Nat. Mater. *18*, 384–389.

33. Gao, Y., Zhao, Y., Li, Y., Huang, Q., Mallouk, T., and Wang, D. (2017). Interfacial chemistry regulation via a skin-grafting strategy enables high-performance lithium-metal batteries. J. Am. Chem. Soc. *139*, 15288–15291.

34. Cheng, X.B., Zhang, X.Q., Liu, H., and Zhang, Q. (2018). Electronic and ionic channels in working interfaces of lithium metal anodes. ACS Energy Lett. *3*, 1564–1570.

35. Vaughey, J.T., Liu, G., and Zhang, J.G. (2014). Stabilizing the surface of lithium metal. MRS Bull. *39*, 429–435.

36. Yan, C., Cheng, X.B., Tian, Y., Chen, X., Zhang, X.Q., Li, W.J., Huang, J.Q., and Zhang, Q. (2018). Dual-layered film protected lithium metal anode to enable dendrite-free lithium deposition. Adv. Mater. *30*, 1707629.

37. Meng, X., Yang, X.Q., and Sun, X. (2012). Emerging applications of atomic layer deposition for lithium-ion battery studies. Adv. Mater. *24*, 3589–3615.

38. Zhao, Y., and Sun, X. (2018). Molecular layer deposition for energy conversion and storage. ACS Energy Lett. *3*, 899–914.

39. Zhao, Y., Zheng, K., and Sun, X. (2018). Addressing interfacial issues in liquid-based and solid-state batteries by atomic and molecular layer deposition. Joule *2*, 2583–2604.

40. Lu, L.L., Ge, J., Yang, J.N., Chen, S.M., Yao, H.B., Zhou, F., and Yu, S.H. (2016). Free-standing copper nanowire network current collector for improving lithium anode performance. Nano Lett. *16*, 4431–4437.

41. Zhao, Y., Goncharova, L., Lushington, A., Sun, Q., Yadegari, H., Wang, B., Xiao, W., Li, R., and Sun, X. (2017). Superior stable and long life sodium metal anodes achieved by atomic layer deposition. Adv. Mater. *29*, 1606663.

42. Zhao, Y., Goncharova, L., Zhang, Q., Kaghazchi, P., Sun, Q., Lushington, A., Wang, B., Li, R., and Sun, X. (2017). Inorganic-organic coating via molecular layer deposition enables long life sodium metal anode. Nano Lett. *17*, 5653–5659.

43. Meng, X. (2017). An overview of molecular layer deposition for organic and organic–inorganic hybrid materials: mechanisms, growth characteristics, and promising applications. J. Mater. Chem. A *5*, 18326–18378.

44. Gao, Z., and Qin, Y. (2017). Design and properties of confined nanocatalysts by atomic layer deposition. Acc. Chem. Res. *50*, 2309–2316.

45. Meng, X., Wang, X., Geng, D., Ozgit-Akgun, C., Schneider, N., and Elam, J.W. (2017). Atomic layer deposition for nanomaterial synthesis and functionalization in energy technology. Mater. Horiz. *4*, 133–154.

46. Chen, L., Connell, J.G., Nie, A., Huang, Z., Zavadil, K.R., Klavetter, K.C., Yuan, Y., Sharifi-Asl, S., Shahbazian-Yassar, R., Libera, J.A., et al. (2017). Lithium metal protected by atomic layer deposition metal oxide for high performance anodes. J. Mater. Chem. A *5*, 12297–12309.

47. Xiao, W., Hui, D., Zheng, C., Yu, D., Qiang, Y., Ping, C., Xiang, C., and Yi, Z. (2015). A flexible transparent gas barrier film employing the method of mixing ALD/MLD-grown Al_2O_3 and alucone layers. Nanoscale Res. Lett. *10*, 130.

48. Yoon, K., Kim, H., Han, K., Kim, S., Lee, Y., Shrestha, N., Song, S., and Sung, M. (2017). Extremely high barrier performance of organic-inorganic nanolaminated thin films for organic light-emitting diodes. ACS Appl. Mater. Interfaces *9*, 5399–5408.

49. Sundberg, P., and Karppinen, M. (2014). Organic and inorganic-organic thin film structures by molecular layer deposition: a review. Beilstein J. Nanotechnol. *5*, 1104–1136.

50. Piper, D., Travis, J., Young, M., Son, S.B., Kim, S., Oh, K., George, S., Ban, C., and Lee, S.H. (2014). Reversible high-capacity Si nanocomposite anodes for lithium-ion batteries enabled by molecular layer deposition. Adv. Mater. *26*, 1596–1601.

51. Peng, Q., Gong, B., VanGundy, R., and Parsons, G. (2009). "Zincone" zinc oxide-organic hybrid

polymer thin films formed by molecular layer deposition. Chem. Mater. *21*, 820–830.

52. Park, Y., Kim, H., Cho, B., Lee, C., Choi, S., Sung, M., and Lee, J. (2016). Intramolecular and intermolecular interactions in hybrid organic-inorganic alucone films grown by molecular layer deposition. ACS Appl. Mater. Interfaces *8*, 17489–17498.

53. Ban, C., and George, S. (2016). Molecular layer deposition for surface modification of lithium-ion battery electrodes. Adv. Mater. Interfaces *3*, 1600762.

54. Cao, C., Mukherjee, S., Liu, J., Wang, B., Amirmaleki, M., Lu, Z., Howe, J.Y., Perovic, D., Sun, X., Singh, C.V., et al. (2017). Role of graphene in enhancing the mechanical properties of TiO_2/graphene heterostructures. Nanoscale *9*, 11678–11684.